ADVANCED MATERIALS
www.advmat.de

Topology Fortified Anodes Powered High-Energy All-Solid-State Lithium Batteries

Xinxin Zhang, Hailong Yu, Liubin Ben, Guanjun Cen, Yang Sun, Liping Wang, Junfeng Hao, Jing Zhu, Qiangfu Sun, Ronghan Qiao, Xiayin Yao, Heng Zhang,* and Xuejie Huang**

Despite its high theoretical capacity and the lowest electrode potential, the lithium metal (Li°) anode possesses significant volume changes and narrow external pressure tolerance upon cycling, hindering its commercial applications in all-solid-state lithium batteries (ASSLBs). Herein, the concept of topology fortified anode (TFA) materials is introduced, featuring a 3D lithiophilic Li_5B_4 skeleton combined with an ingeniously optimized fraction of electroactive lithium phase, along with broadened external pressure tolerance to synergistically enhance the electrochemical performance of ASSLBs. The unique topological design of the TFA materials empowers them with robust mechanical stability and fast lithium diffusivity, achieving near-zero volume changes along with a fivefold improvement in external pressure tolerance compared to Li°. An archetypal TFA-based symmetric cell demonstrates 3.6-fold higher critical current density than its Li°-based counterpart, sustaining stable cycling for >6,000 h at 2 mAh cm^{-2}. When paired with a high-capacity of FeS_2 cathode, the archetypal TFA-based full cells achieve 62% active lithium utilization (9.5 mAh cm^{-2}), and ≈70% capacity retention after 800 cycles at a high current density of 3.07 mA cm^{-2}. The findings provide a revolutionary design approach for high-energy anodes in ASSLBs, advancing not only their development but also battery technologies beyond lithium chemistry.

1. Introduction

Lithium metal (Li°), with its high theoretical capacity (3860 mAh g^{-1}) and the lowest electrode potential (−3.04 V vs the standard hydrogen electrode), is considered as a promising anode material for high-energy rechargeable lithium batteries.[1] All-solid-state lithium batteries (ASSLBs) employ inorganic and organic solid electrolytes instead of flammable and flowable liquid electrolytes, thereby enhancing their intrinsic safety.[2] Furthermore, the superior energy density of ASSLBs meets the demands of electric vehicles and large-scale energy storage systems, establishing them as a key strategy for advancing next-generation high-specific-energy batteries.

For conventional lithium-ion batteries (LIBs), nonaqueous liquid electrolytes can effectively penetrate and fill the porous fractions in both polymeric separators and composite electrode materials without requiring external pressure, owing to the high fluidity and wettability of the selected liquid components (**Figure 1a**). However, this advantageous scenario faces a strong hindrance in solid-state configurations. The non-flowable nature of solid electrolytes in ASSLBs necessitates the application of external pressure during cell assembly, formation, and even cycling. This pressure counteracts varying magnitudes of volume changes for both cathode and anode materials, thereby preserving efficient ionic and electronic transport pathways

X. Zhang, H. Yu, L. Ben, G. Cen, J. Hao, J. Zhu, Q. Sun, X. Huang
Beijing National Laboratory of Condensed Matter Physics
Chinese Academy of Sciences
Institute of Physics
Beijing 100190, China
E-mail: benliubin@iphy.ac.cn; xjhuang@iphy.ac.cn

X. Zhang, H. Yu, L. Ben, G. Cen, J. Hao, J. Zhu, Q. Sun, R. Qiao, X. Yao, X. Huang
Center of Materials Science and Optoelectronics Engineering
University of Chinese Academy of Sciences
Beijing 100049, China

L. Ben, X. Huang
Songshan Lake Materials Laboratory
Dongguan, Guangdong 523808, China

The ORCID identification number(s) for the author(s) of this article can be found under https://doi.org/10.1002/adma.202506298

DOI: 10.1002/adma.202506298

Y. Sun
School of Materials
Sun Yat-sen University
Shenzhen, Guangdong 518107, China

L. Wang
School of Materials and Energy
University of Electronic Science and Technology of China
Chengdu, Sichuan 611731, China

R. Qiao, X. Yao
Ningbo Institute of Materials Technology and Engineering
Chinese Academy of Sciences
Ningbo, Zhejiang 315201, China

H. Zhang
Key Laboratory of Material Chemistry for Energy Conversion and Storage
Ministry of Education
School of Chemistry and Chemical Engineering
Huazhong University of Science and Technology
Wuhan, Hubei 430074, China
E-mail: hengzhang2020@hust.edu.cn

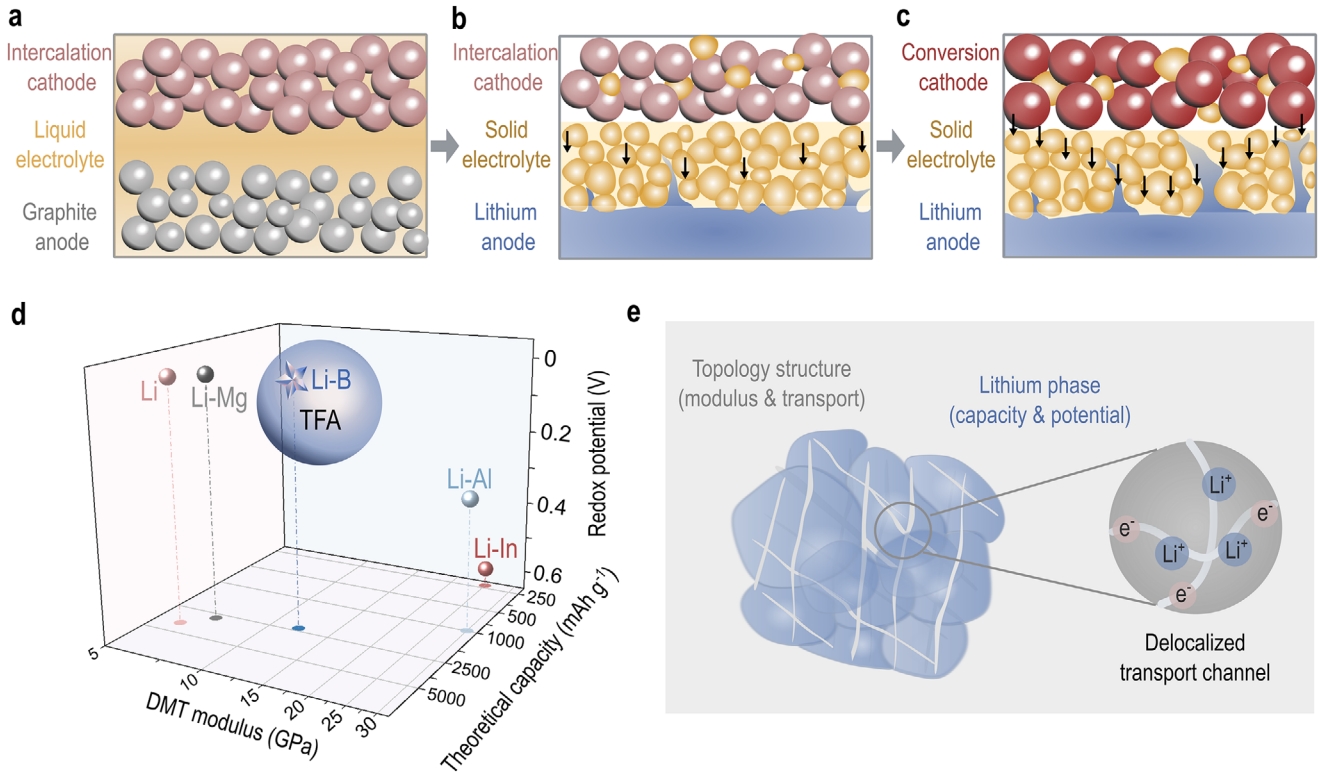

Figure 1. Design concept of topology fortified anode (TFA) materials for high-performance ASSLBs. a–c) Schematic diagrams of (a) conventional LIBs, (b) popular ASSLBs employing intercalation-type cathode materials, and (c) emerging ASSLBs containing conversion-type cathode materials. d) Specific requirements of anode materials for ASSLBs, including DMT modulus (see Supporting Information for details), redox potentials, and theoretical capacities. Representative anode materials are compared, with source data compiled in Table S1 (Supporting Information). e) Schematic of the proposed archetypal TFA material, featuring a skeleton structure that enables delocalized ion and electron transport pathways while maintaining robust mechanical properties.

during continuous cycling (Figure 1a–c).[3] For typical examples, intercalation-type cathode materials generally require a relatively low pressure of a few hundred of kilopascal,[4] with volume changes usually as low as 10%.[5] However, the external pressure surges to several tens of megapascals when the intercalation-type cathode materials are replaced with high-capacity conversion-type cathode materials,[6] since the latter suffers from higher volume change during lithiation and delithiation processes.[7]

To ensure sufficient physical contact between electrode materials and electrolyte components, it has been commonly accepted that an adequate external pressure is essential for the cell assembly and cycling.[8] However, the neat Li° anode exhibits significant sensitivity toward external pressure.[9] Under a pressure of a few tens of megapascals, the neat Li° anode gradually infiltrates into the existing pores and cracks of the solid electrolyte, which may act as preferred nucleation sites for subsequent electrochemical depositions. This process leads to pressure-induced Li° intrusion issues,[10] a growing threat that escalates with elevating external pressure. At increased pressures, a detrimental internal short circuit immediately occurs after the cell assembly due to the electronic channels provided by interconnected Li° phases filled in the solid electrolyte film.[10b] Adding to the hurdles in mechanical strength, the Li° anode in bulk sheet form offers exceedingly limited transport channels for lithium diffusion as compared to the nano-sized graphite materials being used in today's LIBs. This limitation leads to sluggish redox kinetics and inhomogeneous lithium plating and stripping.[11] Consequently, there is a strong demand to optimize the anode topology to meet the specific operational requirements of ASSLBs.[12]

Significant advances in the compositional and architectural design of anode materials have been achieved to improve the electrochemical performance of ASSLBs. Anode materials that integrate electroactive Li° phase with inactive framework materials (e.g., carbon, silicon, indium, and tin etc.) have demonstrated enhanced mechanical strength and accelerated lithium transport.[13] For example, the addition of silicon or indium greatly improves the mechanical strength of anode materials, even after lithiation,[14] while the incorporation of carbon and other materials into the neat Li° anode or its alloys enhances lithium diffusion rates.[15] However, the increased electrode potential of these composite anode materials, together with the presence of excessive inactive components, leads to a certain degree of reduction in specific capacity, which unfortunately impairs their promised advantages in energy and power density over conventional LIBs.[13a,16]

In this work, we present the design concept of topology fortified anode (TFA) materials as a "crackpot" approach to counteract the negative impacts provoked by non-electroactive phases in anodes, while providing desired mechanical strength and diffusive properties. This design enables robust cell assembly and

cycling of ASSLBs under a broader range of external pressures (Figure 1d). The topological fortification is achieved by an ingeniously designed skeleton structure, which provides not only exceptional mechanical properties but also superior lithiophilicity and additional transport channels for lithium ions and electrons. As a prototype, the conceptual design of the TFA materials is demonstrated by a specifically tailored lithium–boron (Li–B) alloy, comprising ≈60 wt.% of "free" Li° phase embedded within a robust 3D fibrous skeleton structure (Figure 1e). In this archetypal TFA material, the 3D fibrous skeleton exhibits outstanding mechanical strength, ensuring the structural integrity of the anode over extended cycling. Its lithiophilic feature facilitates efficient electrochemical plating and stripping processes and enables rapid lithium transport. Furthermore, the optimized fraction of electroactive Li° phase ensures a low redox potential close to that of pristine Li°, while simultaneously delivering a high theoretical specific capacity exceeding 2000 mAh g^{-1} (based on the total anode mass, Figure 1d). Notably, unlike previous reports of Li–B alloy applications in liquid electrolytes,[17] the archetypal TFA material, with its preciously tailored Li content, perfectly meets the unique operational requirements (e.g., mechanical stability and electrochemical properties) of ASSLBs.

2. Results and Discussion

2.1. Fundamental Properties of TFA

The chemical structure and physical properties of the proposed archetypal TFA material were systematically investigated using a combination of mesoscale characterization techniques. The "free" Li° phase in the TFA material was chemically removed by reacting with naphthalene in anhydrous tetrahydrofuran solution (*cf.* Experimental Methods).[18] This chemical delithiation process exposed the TFA skeleton for further chemical and morphological characterizations. X-ray diffraction (XRD) measurements revealed that the as-obtained TFA skeleton showed several diffraction peaks, consistent with the standard profile of Li_5B_4. The bulk TFA material exhibited a combination of diffraction peaks assigned to both the Li° phase and the Li_5B_4 skeleton (**Figure 2a**). As seen in Figure 2b,c, the TFA skeleton, exposed after the chemical delithiation, appeared a 3D fibrous network structure with fiber diameters ranging from ≈100 to 400 nm. The overall morphology of the skeleton at larger scales is illustrated in Figure S1 (Supporting Information). These results confirm that the archetypal TFA material is majorly composed of a "free" Li° phase and a fibrous Li_5B_4-rich skeleton. The Li–B phase diagram reported by Marcac and co-workers is also shown in Figure S2 (Supporting Information).[19]

By implementing the Derjaguin–Muller–Toporov (DMT) model in atomic force microscopy (AFM), the mechanical properties of the bulk TFA material and its fibrous skeleton were quantitatively analyzed (Figure S3, Supporting Information).[20] For the pristine Li° electrode, the DMT profile centered at a relatively low modulus value of ≈6.5 GPa with a typical Gaussian distribution [≈2.94 for full width at half maximum (FWHM), Figure 2d]. Such low modulus values explain the pressure-induced penetration and undesired growth of Li° dendrites in ASSLBs employing the pristine Li° electrode.[10] In stark contrast, the fibrous skeleton of the TFA electrode showed DMT modulus ranging from 10 to 50 GPa, significantly higher than those for the pristine Li° electrode. The presence of the fibrous Li_5B_4-rich skeleton substantially enhances the mechanical stability of the bulk TFA material, as reflected by its higher DMT modulus (≈12.8 GPa). Very interestingly, the distribution of DMT modulus for the bulk TFA material aligned the pattern observed for the TFA skeleton, suggesting that these two phases collectively fulfill the specific mechanical properties requirements, capacity, and voltage characteristics essential for ASSLBs (*cf.* **Figure 3e**).

To simulate the cell assembly and testing condition, the TFA and pristine Li° electrodes were separately paired with the same solid electrolyte (i.e., Li_6PS_5Cl) under different external pressures (Figure 2e). As shown in Figure 2f, under an external pressure of 50 MPa, the reference Li° electrode gradually infiltrated into the pores and cracks within the solid electrolyte, leading to mechanical fracture of the solid electrolyte and significant surface inhomogeneity at the electrode-electrolyte interphase. Additional evidence supporting lithium metal penetration into the electrolyte is provided in Figures S4 and S5 (Supporting Information). Under the same pressure, the TFA electrode maintained sufficient physical contact with the solid electrolyte after pressing without infiltrating into the inherent pores and cracks of the bulk electrolyte (Figure 2g). This clearly testifies the high modulus of the TFA skeleton is beneficial for ensuring the structural integrity of the TFA material during the cell assembly and cycling. It is important to highlight that the weight fraction of the "free" Li° phase greatly affect the mechanical properties of the TFA material. A lithium-like response (i.e., mechanical creep) to external pressure was observed with an excessive amount of the "free" Li° phase (>70 wt.%, Figure S6, Supporting Information). Therefore, both the "free" Li° phase and the fibrous Li_5B_4-rich skeleton should be rigorously regulated to maximize the power of topological fortification provided by the TFA concept.

In addition to the aforesaid mechanical properties, the unique diffusion behavior of the archetypal TFA material is another key factor in enabling reversible cycling in ASSLBs. To explore this, density functional theory (DFT) calculations were performed to investigate the chemical affinity between the Li° and Li_5B_4 skeleton. Stable Li (001) and Li_5B_4 (110) surfaces were established to understand lithium deposition behavior on the Li° and Li_5B_4 skeleton. Different adsorption sites were selected based on symmetry, and the adsorption energies of Li at these sites were calculated, as shown in Figure 3a. The adsorption energy of Li on the Li_5B_4 (110) surface was −6.24 eV, which is significantly lower than that (i.e., −1.56 eV) on the Li (001) surface. Specifically, Li atoms around the B site exhibited lower adsorption energy, indicating that lithium deposition within the TFA material is more likely to occur on the Li_5B_4 (110) surface. Compared to the single-phase Li°, the presence of the Li_5B_4 skeleton renders the TFA material with a superior lithiophilic nature, facilitating more uniform lithium deposition within the material.

Next, ab initio molecular dynamics (AIMD) simulations were conducted on the Li° and Li_5B_4 skeleton to study the dynamic behavior of Li atoms within the TFA material (Figure 3b). At a simulation temperature of 300 K, the mean square displacement (MSD) of Li atoms in the "free" Li° phase showed insignificant changes over time, while the MSD values of Li atoms in the Li_5B_4 skeleton increased significantly over the same period. This indicates faster diffusion capabilities for Li atoms in the

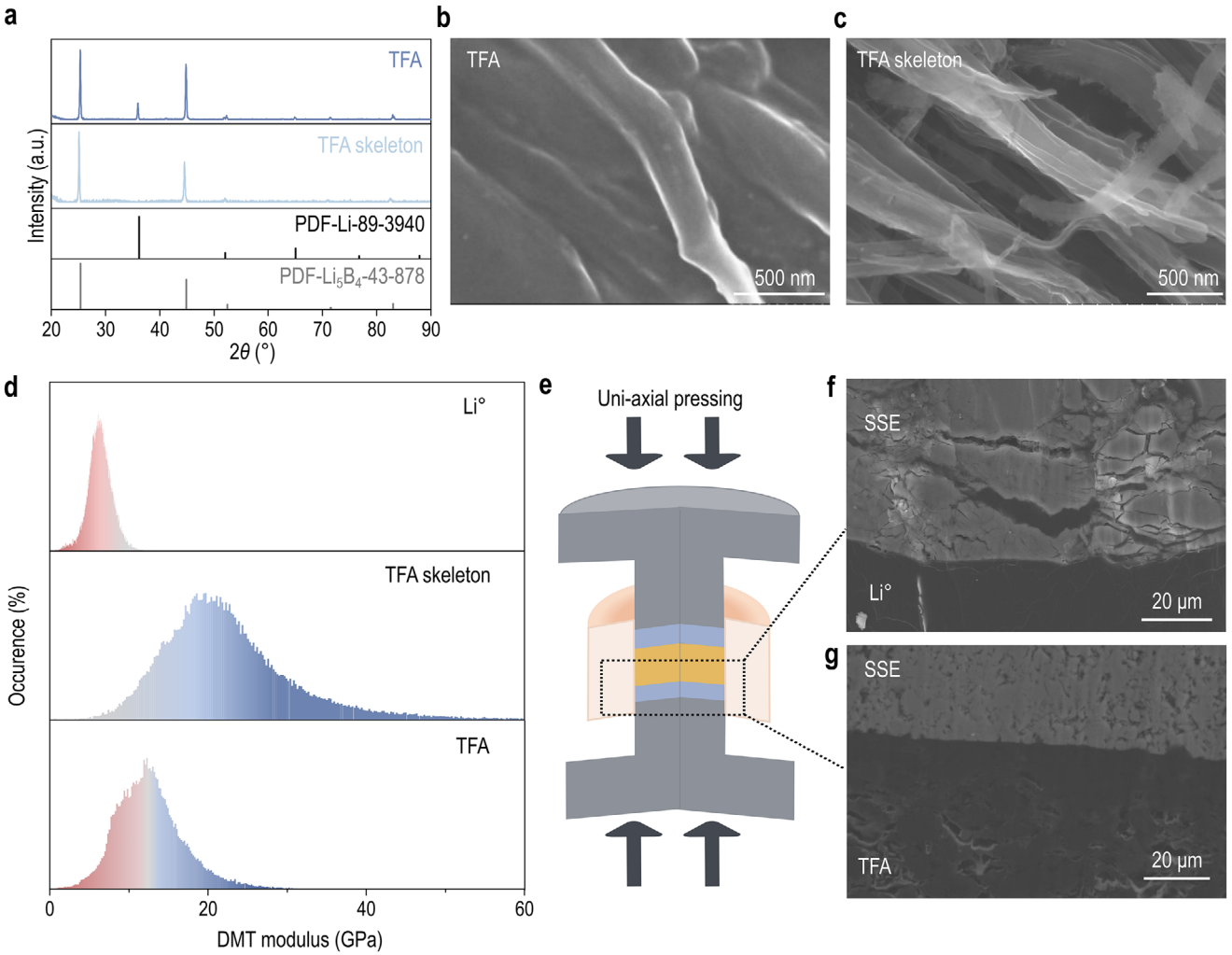

Figure 2. Fundamental physical properties of TFA materials. a) XRD patterns of the archetypal TFA material and its skeleton, compared to standard profiles of Li° (PDF-Li-89-3940) and Li_5B_4 (Li_5B_4-43-878). b,c) Cross-sectional SEM images of b) the archetypal TFA material and c) its skeleton. d) DMT modulus obtained from AFM tests for the pristine Li°, archetypal TFA material, and its skeleton. e) Schematic diagram of the mold cell subjected to external pressure. f,g) Cross-sectional SEM images of the (f) pristine Li° and (g) the archetypal TFA material under an external pressure of 50 MPa.

Li_5B_4 skeleton versus neat Li°. To further illustrate the diffusion process, structural diagrams of the Li° and Li_5B_4 skeleton at 0 and 20 ps were generated, as shown in Figure S7 (Supporting Information). Analysis of these structural diagrams reveals that Li atoms in the Li° remain close to their equilibrium positions, exhibiting minimal diffusion. In contrast, the Li_5B_4 skeleton facilitates Li diffusion by forming continuous long-chain clusters through boron atoms, thereby creating ordered channels for lithium transport.[21]

Utilizing isotopic tracing in time-of-flight second ion mass spectroscopy (ToF-SIMS), we determined the lithium diffusion coefficients within both the Li° and TFA material (Figure S8, Supporting Information). The concentration of the isotopic tracer was fitted using the Gaussian solution of Fick's second law (*cf.* Experimental Methods). The diffusion profiles of the isotope ^{6}Li in the ^{7}Li-based Li° and the TFA electrodes are presented in Figure 3c,d, from which the diffusion coefficient of lithium (D_{Li}) was calculated (Equation 2). The D_{Li} value obtained for the TFA electrode is one order of magnitude higher than that with the neat Li°, e.g., 2.4×10^{-10} (TFA) versus 2.5×10^{-11} cm^2 s^{-1} (Li°) at room temperature. The results of computational simulations and ToF-SIMS experiments suggest that the lithophilic properties and superior dynamic transmission characteristics of the fibrous skeleton enable the TFA material to achieve rapid Li plating and stripping during electrochemical tests (*cf.* Section 2.2).

To ensure their application in ASSLBs, the selected anode materials should maintain tantalizing electrochemical features, including low redox potential, facile lithium nucleation, and fast lithium diffusion.[15a,22] Therefore, the fundamental electrochemical properties of the TFA material were thoroughly investigated, with the results provided in Figure 3e and Figure S9 (Supporting Information). Voltage-capacity profile (Figure 3e) shows that the TFA electrode exhibited a flat plateau at a low voltage value of ≈0 V (vs Li/Li$^+$), corresponding to the stripping of the "free" Li° phase, while the plateau ≈0.8 V is linked to the phase evolution of the Li_5B_4 skeleton.[23] Cross-sectional images

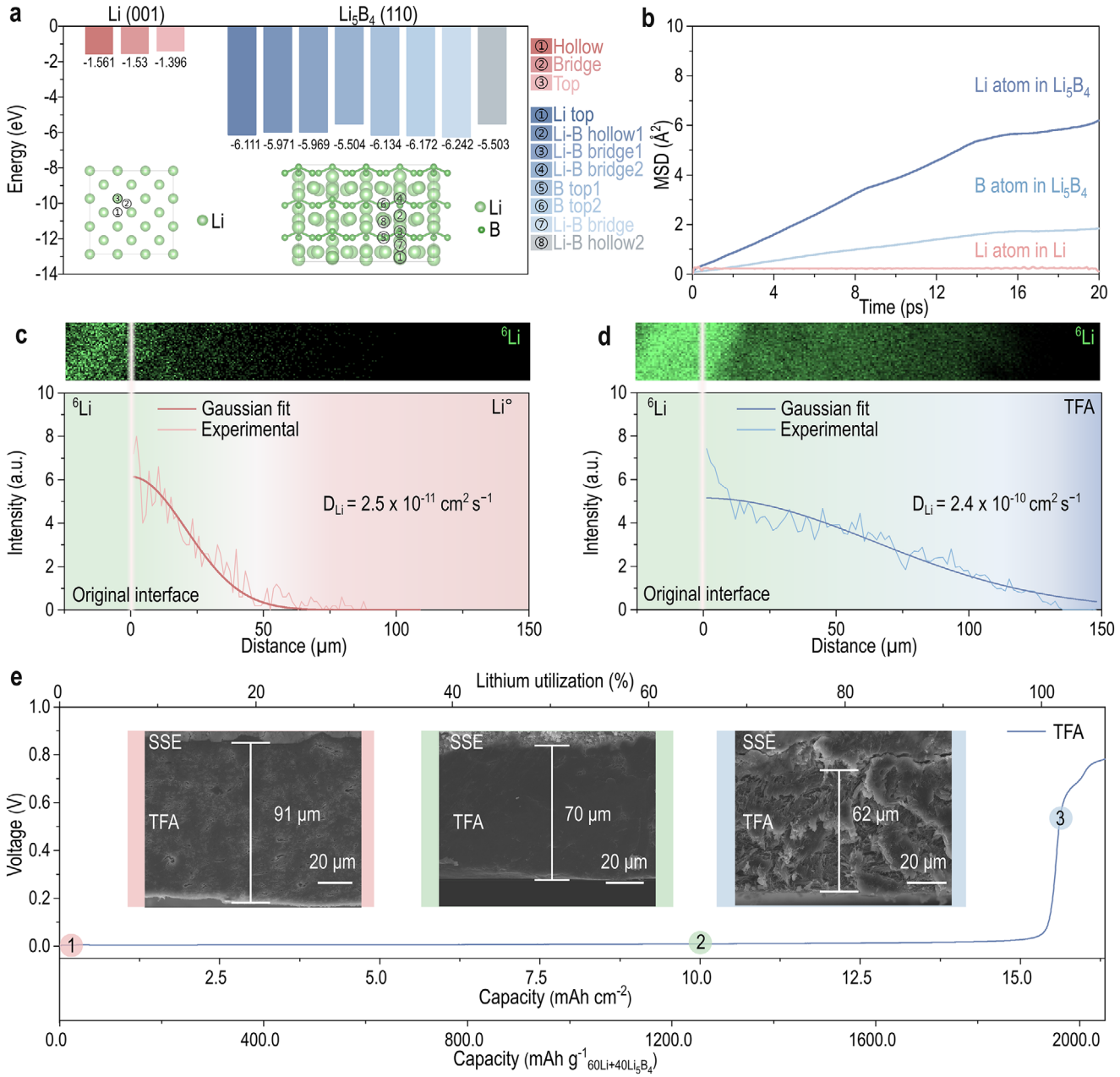

Figure 3. Electrochemical features of TFA materials for practical ASSLBs. a) Calculated Li absorption energies on Li (001) and Li_5B_4 (110) surfaces. b) MSD plots of Li and B atoms in Li and Li_5B_4 obtained by ab initio molecular dynamics (AIMD) simulations at 300 K. c,d) ToF-SIMS diffusion profiles of ^6Li tracer isotopes in the (c) Li° and (d) archetypal TFA electrodes. e) SEM images and voltage profile of the archetypal TFA electrodes obtained in a symmetric cell.

measured by scanning electron microscopy (SEM) revealed that an intimate physical contact between the TFA electrode and the solid electrolyte was maintained under moderate lithium utilization (≈10 mAh cm^{-2}, stage 2 in Figure 3e, with complementary regional analyses provided in Figure S10a–d, Supporting Information). However, excessive stripping of lithium from the TFA material results in contact failure of the anode compartment, accompanied by the structural collapse of the TFA skeleton (stage 3 in Figure 3e; Figure S10e,f, Supporting Information). Therefore, the degree of electroactive lithium utilization from the TFA material needs to be carefully restrained to allow reversible electrochemical stripping and plating processes in ASSLBs. In this scenario, the present archetypal material of the TFA concept (i.e., Li–B alloy containing 60 wt.% "free" Li° phase) provides a specific capacity of 1926 mAh g^{-1} at the material level, but a maximum utilization degree of 65% is recommended for practical cell testing. Nonetheless, the attainable specific capacity of the TFA material remains among the highest reported for anode materials designed for ASSLBs reported in literature (*cf* Figure 1d).

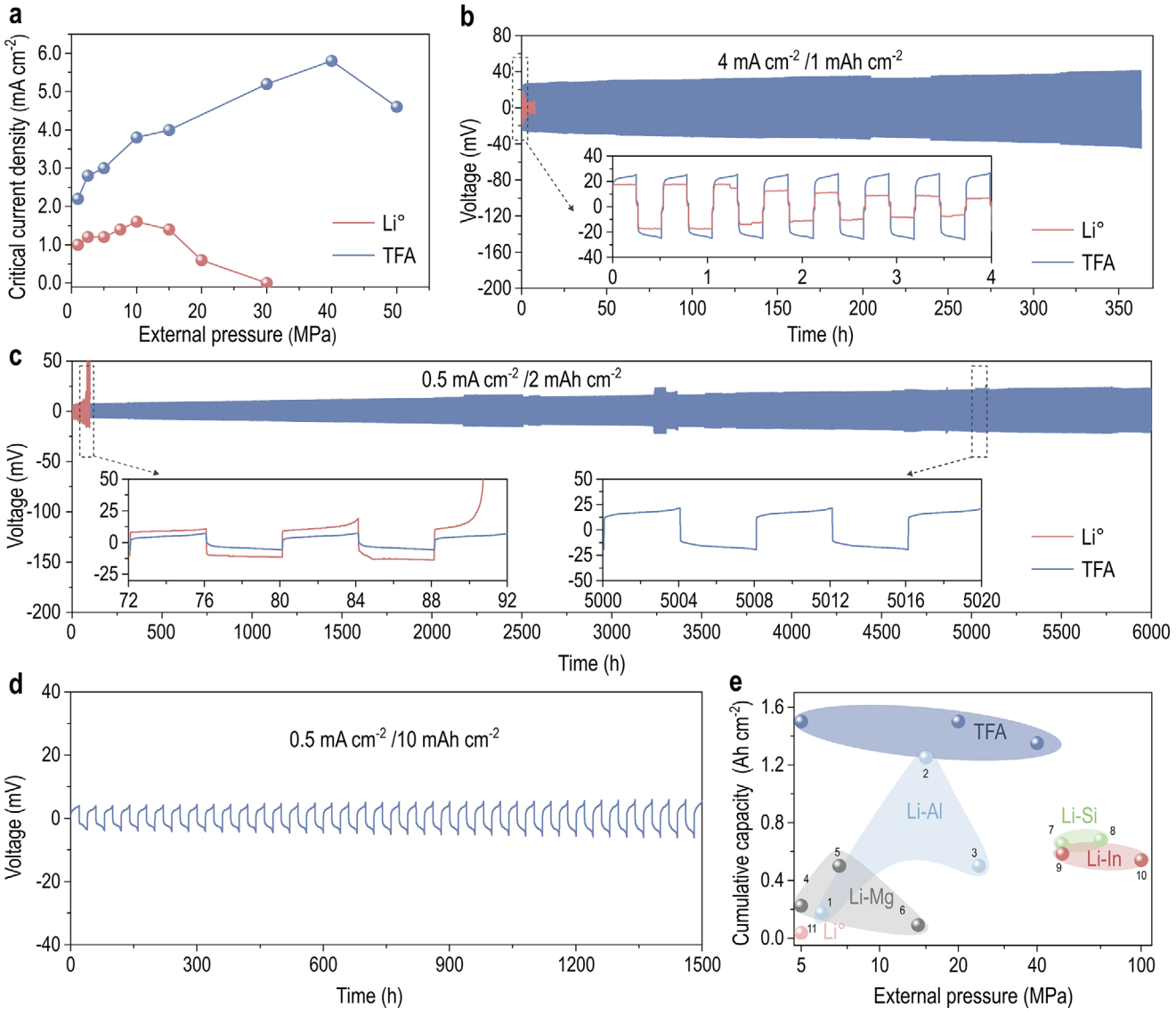

Figure 4. Electrochemical performances of TFA-based symmetric cell under varied external pressures. a) Critical current density (CCD) of the TFA- and Li°-based symmetric cells as a function of external pressure. b,c) Galvanostatic cycling profiles of the TFA- and Li°-based symmetric cells under distinct current densities and capacities: b) 4 mA cm^{-2} with an areal capacity of 1 mAh cm^{-2} and c) 0.5 mA cm^{-2} with an areal capacity of 2 mAh cm^{-2}. d) Galvanostatic cycling of the TFA-based symmetric cell at 0.5 mA cm^{-2} with an areal capacity of 10 mAh cm^{-2}. e) Cumulative areal capacity and external pressures achieved with TFA-based symmetric cell and those reported in literature (Table S2, Supporting Information).

2.2. Feasibility of TFA for ASSLBs

To validate the feasibility of the TFA material in ASSLBs, its electrochemical performance was characterized using symmetric cell configurations under stringent conditions (i.e., high areal capacities, various external pressures). Critical current density (CCD) is widely regarded as an essential indicator of anode tolerance under high-power working conditions.[24] For a conventional Li°-based symmetric cell, modest CCD values (≈1.6 mA cm^{-2}) were achieved at an external pressure of ≈10 MPa, while a significant drop in CCD values was noticed at higher external pressures (e.g., 0.6 mA cm^{-2} at 20 MPa). Moreover, the Li°-based symmetric cell experienced mechanical short-circuiting under a pressure of 30 MPa. In stark contrast, the CCD values of the TFA-based symmetric cell were significantly higher than those of the Li° reference cell across a wide pressure range of 0–50 MPa (**Figure 4a**; Figure S11, Supporting Information). The maximum CCD value of the TFA-based symmetric cell reached 5.8 mA·cm^{-2}, which is 3.6 times greater than that of the Li° reference cell. Even at room temperature, the TFA-based symmetric cell achieved a CCD of 2.6 mA cm^{-2}, tripling the performance of the pristine Li° anode under identical conditions (Figure S12, Supporting Information). The improved CCD values for the TFA-based symmetric cell highlight the critical role of the architectural design of anode materials in achieving high cycling capacity and current density. Cycling tests conducted at various external pressures further demonstrated that the TFA-based symmetric cell exhibited superior cycling performance compared to the Li° reference cell

(Figure S13, Supporting Information). This can be attributed to the key tantalizing features of the TFA material, including high mechanical strength, lithiophilic nature, and fast diffusivity of lithium.

To further confirm the long-term cycling stability, the cycling performance of the TFA-based symmetric cell was tested at a moderate external pressure (20 MPa), as shown in Figure 4b–d. Notably, the TFA-based symmetric cell demonstrated successful cycling for over 350 h at a current density of 4 mA·cm^{-2} (Figure 4b), whereas the Li° reference cell experienced a sudden drop in overpotential after only a few hours, indicating short-circuiting caused by lithium dendrite penetration.[25] The Li°-based reference cell exhibited polarization growth exceeding 50 mV after only 80 h of cycling at 2 mAh cm^{-2}, followed by a sudden voltage drop due to a short circuit. The sharp increase in impedance is attributed to the formation of numerous pores at the interface, leading to contact failure. The reduced number of effective contact points results in non-uniform lithium deposition, culminating in a short circuit. In contrast, the TFA-based symmetric cell exhibited a stable cycling profile for over 6,000 h at a high areal capacity of 2 mAh cm^{-2}, maintaining a consistent voltage plateau during lithium plating and stripping. The overpotential stabilized at 10 mV after 80 h of cycling and increased only slightly to 20 mV after 5,000 h (Figure 4c). The transient overpotential increase observed in 3,200–3,500 h likely reflects minor temperature fluctuations and interfacial evolution during the extended (>250 day) testing period. To optimize lithium accommodation during high-areal capacity cycling, a pre-extraction strategy was employed to partially remove the "free" lithium phase in the TFA electrode (cf. Figure S14, Supporting Information). Remarkably, even under extreme conditions (e.g., 10 mAh·cm^{-2}), the TFA-based symmetric cell maintains stable cycling with a lithium utilization rate exceeding 65% (Figure 4d). Furthermore, the TFA-based symmetric cell displayed stable cycling exceeding 6,000 h with a capacity of 2 mAh cm^{-2} at a minimal pressure of 5 MPa and over 1,350 h at 2 mA cm^{-2} under a higher external pressure of 40 MPa (Figures S15 and S16, Supporting Information). Compared to other alloy anodes, such as Li—Mg, Li—Al, and Li—Si (Table S2, Supporting Information), the TFA-based symmetric cell exhibited an extremely high cumulative capacity and superior tolerance to a broad range of external pressures (Figure 4e).

2.3. Working Mechanism of TFA in ASSLBs

To elucidate the working principle behind the superior electrochemical behavior of the TFA concept, detailed mechanistic studies were performed. **Figure 5**a–d shows the cross-sectional SEM images of the cycled TFA and Li° electrodes from symmetric cells (current density: 0.5 mA cm^{-2}, areal capacity: 5 mAh cm^{-2}). The thickness change of the TFA electrode remained less than 10 µm, while the thickness change of the Li° electrode was ≈25 µm (Figure S17, Supporting Information). Detailed statistics on these thickness changes are available in Figures S18,S19, and Table S3 (Supporting Information). This indicates that the volume change of the TFA electrode is only 40% of that of the pristine Li° counterpart under the same experimental conditions. The volume changes of the electrodes during charge and discharge cycles can also be reflected by the increase or decrease in internal pressure.[26] The TFA electrode exhibited significantly reduced volume changes, leading to a decrease in pressure variations from 0.36 to 0.28 MPa during ASSLBs cycling, as detected by in situ pressure monitoring devices (Figure S20, Supporting Information).

The excessive volume change of the Li° electrode exacerbates inhomogeneous plating and stripping. As shown in Figure 5c, the TFA electrode remained intact after stripping large areal capacities, and its interface with the electrolyte remained flat and tightly contacted as in its initial state. In contrast, the interface of the Li° electrode deteriorated significantly after stripping, resulting in pores and a loss of physical contact (Figure 5a). Poor physical contact between the anode and solid electrolyte leads to variation in interface impedance, resulting from volume changes in the anode and inhomogeneous plating and stripping.[27] Through in situ impedance testing on the TFA- and Li°-based symmetric cells (Figures S21 and S22, Supporting Information), as the areal capacity increased, the impedance changes for the TFA-based symmetric cell remained minimal and became even less noticeable over an extended period, while the Li° reference cell showed a monotonic increase in impedance during stripping. Notably, at an areal capacity below 5 mAh cm^{-2}, the impedance of the Li° reference cell reached 20 times that of the TFA-based symmetric cell, e.g., 1.5 Ω cm^2 (TFA) versus 30 Ω cm^2 (Li°). In the Bode plot (Figure S23, Supporting Information), the characteristic frequency of the TFA-based symmetric cell remained at 0.6 Hz during stripping, in stark contrast to the Li° reference cell (which decreases from 0.3 to 0.2 Hz), suggesting a more stable interfacial contact.[28]

As shown in Figure 5b, during the plating process, the deteriorated interface contact induced inhomogeneous Li plating within the solid electrolyte. This contrasts sharply with the uniform Li plating inside the TFA-based system (Figure 5d), which ensures good interfacial contact. Energy dispersive spectrometer (EDS) further demonstrated the structural stability of the TFA skeleton after lithium deposition (Figure S24, Supporting Information). The 3D skeleton in the TFA material ensures dynamic physical contact at the electrode and electrolyte interface, in contrast to the formation of interfacial vacancies in Li° cells. This stable stripping and plating behavior persists even under reduced pressure (5 MPa), where the TFA electrode maintains both structural integrity and interfacial stability after cycling (Figure S25a,b, Supporting Information), confirming the pressure-adaptive nature of the TFA skeleton.

To further investigate the near-zero volume changes of the TFA material, non-destructive X-ray computed tomography (CT) and SEM were employed to analyze the internal structural changes (e.g., porosity and pore distribution) of the aforementioned TFA-based symmetric cell after stripping and plating. In the reconstructed 3D structures, pores within the TFA electrode, indicated by areas of lower X-ray attenuation, were prominently displayed in blue. As shown in Figure 5e and Figure S26 (Supporting Information), the initial porosity of 6.6% enables the TFA structure to accommodate lithium deposition up to ≈2 mAh cm^{-2}. After stripping 5 mAh cm^{-2}, the porosity of the TFA electrode increased from an initial value of 6.6% to 25.7% (Figure 5f), with the size of pores between the internal 3D skeletons of the electrode increasing from 2 to 7 µm (Figure S27a,b, Supporting

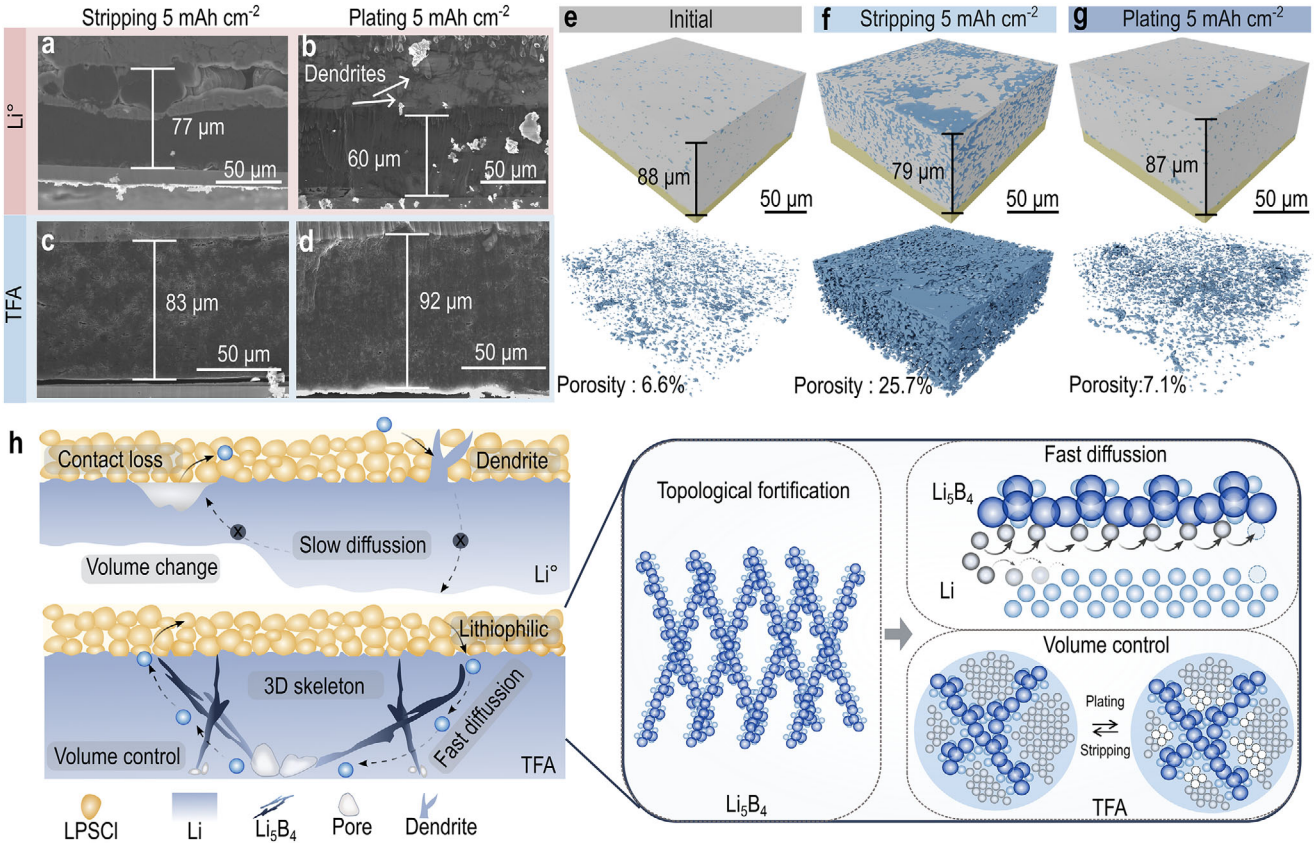

Figure 5. Working principles of TFA materials for improved electrochemical performance. Cross-sectional SEM images of the Li° electrodes: a) after stripping 5 mAh cm^{-2} and b) after plating 5 mAh cm^{-2}. Cross-sectional SEM images of the TFA electrodes: c) after stripping 5 mAh cm^{-2} and d) after plating 5 mAh cm^{-2}. Computed tomography images of the TFA electrodes: e) in initial state, f) after stripping 5 mAh cm^{-2} and g) after plating 5 mAh cm^{-2}. h) Schematic diagram of the plating and stripping processes of the Li° and TFA material.

Information). The enlargement of pore size, along with the increase in porosity, alleviates the volume contraction of the electrode after delithiation. In the subsequent deposition process, lithium re-deposited into the pore structure of the electrode, with a reduced porosity (7.1%, Figure 5g) and a pore size (≈2 μm, Figure S27c, Supporting Information). The newly deposited lithium (Figure S28, Supporting Information) and the evolving pores were evenly distributed around the internal 3D skeleton of the electrode, indicating a uniform internal lithiation and delithiation process. After 100 h of cycling, no significant changes were observed in the internal porosity, electrode thickness, or the quality of interfacial contact compared to the initial state (Figures S27d and S29, Supporting Information). The 3D skeleton structure within the TFA material facilitates the release of "free" Li° from the electrode bulk phase and retains sufficient porosity for subsequent lithium deposition, keeping the overall thickness of the electrode nearly constant even at a high area capacity of 5 mAh cm^{-2}.

As shown in the diagram in Figure 5h, due to poor diffusion kinetics and significant volume changes, the interphase of the pristine Li° electrode without a host structure gradually fails due to the formation of pores in the cycling process. For the TFA-based system, the topological fortification provided by the 3D fibrous skeleton allows adequate preservation and reutilization of the "free" space created by the stripping processes, thereby sustaining superior geometrical reversibility and minimal volume expansion/contraction during operation. In particular, the refilling of "free" space with the electrochemically active Li° phase is made possible by the lithiophilic feature of the interconnected fibrous skeleton, which offers sufficient transport channels for lithium, and thus pumps lithium atoms from the outer interface into the inner compartment of the TFA material during the plating process. Clearly, the TFA concept proposed herein provides a new paradigm for designing electrode materials for future ASSLBs.

In addition, the utilization degree of the "free" Li° phase in the TFA design must be precisely controlled to ensure reversible electrochemical processes. For example, exceeding an areal capacity of 15 mAh cm^{-2} (100% utilization degree) for the present archetypal material of the TFA concept (i.e., the Li–B alloy containing 60 wt.% "free" Li° phase) causes undesired structural collapse of the TFA skeleton. This can trigger the nucleation and growth of the Li° phase between the collapsed TFA skeleton and the solid electrolyte during the subsequent plating process, creating a highly soft and active lithium interlayer that leads to rapid cell failure under electrochemical tests (Figure S30, Supporting Information). For the current application scenario, the TFA material allows a high reversible areal capacity of 10 mAh cm^{-2} (Figures S31 and S32, Supporting Information). To achieve this stable

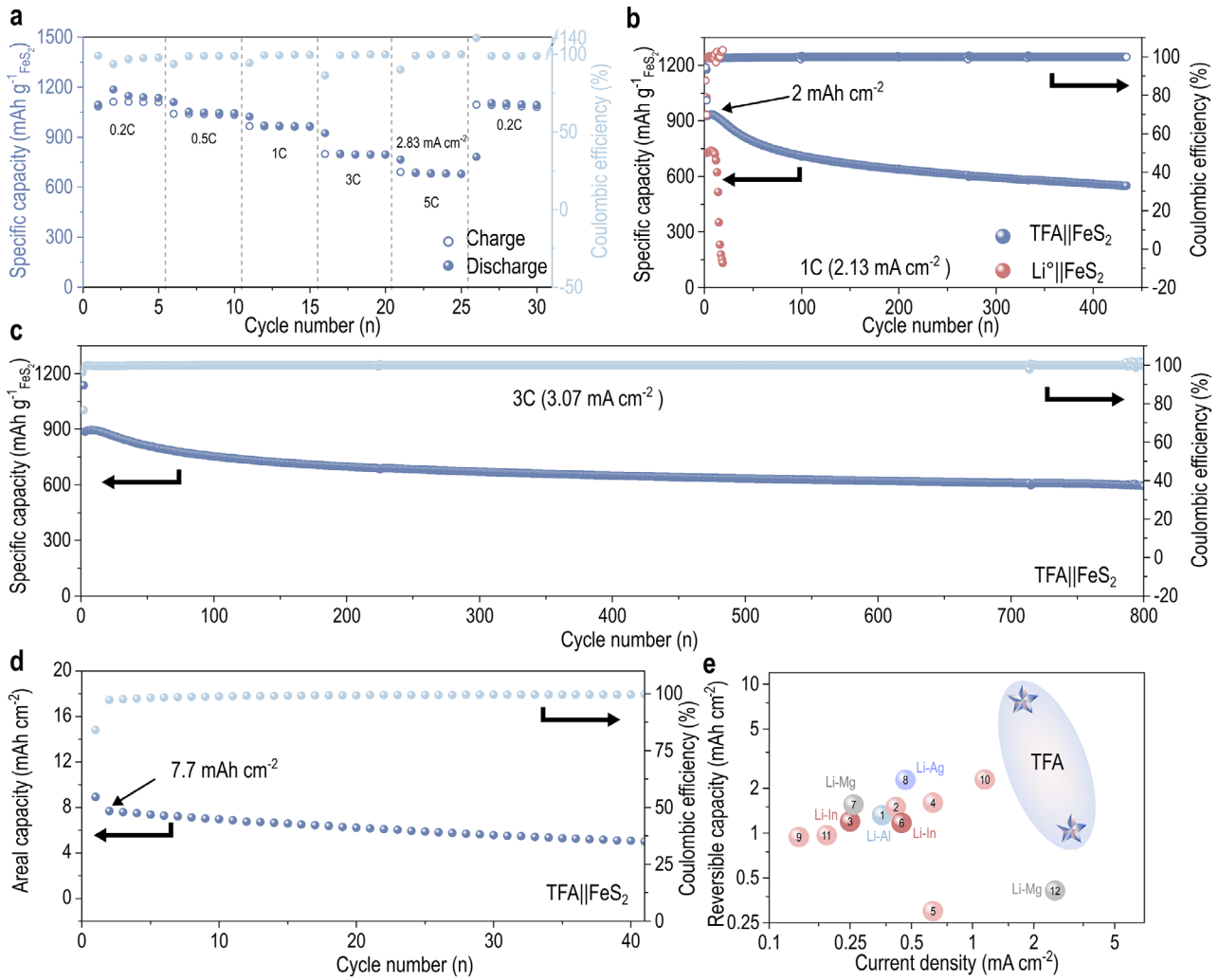

Figure 6. Electrochemical performance of the TFA- and Li°-based full cells paired with FeS_2 cathode. a) Rate performance of the TFA||FeS_2 full cells. Long-term cycling performance of the TFA||FeS_2 full cells with cathode loading of b) 2.17 mg cm^{-2}at 1 C, c) 1.18 mg cm^{-2} at 3 C and d) 9.64 mg cm^{-2} at 0.2 C. e) Comparison of reversible capacity and current density between this work and prior studies (Table S4, Supporting Information).

cycling capacity with the TFA's limited porosity, one approach is pre-treatment to selectively etch "free" Li° phase while preserving the TFA skeleton, creating deposition space. Alternatively, initial stripping using lithium-free cathode full cell configurations can be performed (cf. Section 2.4). After stripping 10 mAh cm^{-2}, the TFA's 3D skeleton shows porosity and enlarged pore size (Figures S10a–d and S33, Supporting Information), while maintaining excellent electrolyte contact (Figure S32a, Supporting Information). Remarkably, lithium preferentially deposits into the internal pores, achieving uniform distribution within the fibrous Li_5B_4-rich skeleton (Figure S32b, Supporting Information). This makes TFA well-matched with high-capacity cathodes for building high-energy ASSLBs.

2.4. Cycling Performance of TFA in ASSLBs

Given the superior electrochemical performances obtained with the TFA material in symmetric cell configurations, we further validated its effectiveness in full cells using a typical conversion-type cathode, iron disulfide (FeS_2), which has high capacity but undergoes significant volume changes during continuous cycling. An external pressure of 40 MPa was applied to ensure efficient ionic and electronic pathways between the active materials in the composite cathode. To further demonstrate the high lithium stripping and deposition capabilities of the TFA material under high external pressure, the rate performances of the TFA||FeS_2 full cell were first evaluated. As shown in **Figure 6**a, the full cell delivered discharge capacities 1133 mAh·g^{-1} at 0.2 C and 1042 mAh·g^{-1} at 0.5 C. Even at a high current density of 5 C (2.83 mA·cm^{-2}), the TFA||FeS_2 full cell delivered a discharge capacity of 677 mAh·g^{-1}, with no signs of short-circuiting. The temporary charge capacity increase at cycle 25 reflects both re-activation of electro-active materials at 0.2 C,[29] and potential concurrent electrochemical reduction of sulfide electrolyte in the composite cathode, which may contribute additional capacity beyond FeS_2's theoretical value.[29a,30] This demonstrates that the high-strength, 3D, and lithiophilic skeleton structure of the TFA material, com-

bined with an ingeniously optimized Li° phase, can meet internal kinetic demands and prevent Li° from invading the electrolyte to form dendrites, even under high current densities. The corresponding charge and discharge curves show consistent shapes across different rates (Figure S34, Supporting Information).

To further confirm the critical role of the TFA material in ASSLBs cycling stability, the cycling performance of the TFA||FeS_2 full cell was examined under different capacities and current densities (Figure 6b–d). Notably, the TFA||FeS_2 full cell stably cycled for 420 cycles with a capacity retention rate of 60% at a reversible capacity of 2 mAh·cm^{-2} and a rate of 1 C, while the reference Li°||FeS_2 full cell experienced short-circuiting after ≈10 cycles. Furthermore, the TFA||FeS_2 full cell exhibited ≈70% capacity retention following 800 cycles under a current density of 3.07 mA·cm^{-2} and stable cycling at an ultrahigh capacity of 7.70 mAh·cm^{-2} for 40 cycles (Figure 6c,d). The enhanced cyclability of the TFA||FeS_2 full cell is attributed to the stability and diffusion characteristics provided by the unique architecture of the TFA material. Specifically, during initial discharge, the "free" Li° phase is stripped from the TFA compartment while maintaining the structural integrity of the 3D network, generating abundant porosity within the TFA electrode. Upon subsequent charging, the lithiophilic TFA skeleton directs homogeneous lithium deposition into these preserved pores (cf. Figure S35, Supporting Information). This mechanism enables high-rate cycling (at a current density of 5.2 mA·cm^{-2}, Figure S36, Supporting Information) and a lithium utilization rate of 62% (at a reversible capacity of 9.5 mAh·cm^{-2}, Figure S37, Supporting Information).

Additionally, leveraging the smaller volume changes of the TFA material, we assembled TFA||$LiNi_{0.93}Co_{0.06}Mn_{0.01}O_2$ (NCM) full cell, which exhibited a smaller volume effect, under an external pressure of 5 MPa. In terms of rate performance (Figure S38, Supporting Information), the full cell withstood a current density of 2.92 mA·cm^{-2} (5 C). During long cycling performance tests, the full cell stably cycled at a specific capacity of 150 mAh·g^{-1} at 0.5 C, retaining 70% of initial capacity after 2000 cycles at 2 C (Figure S39, Supporting Information). This enhanced cycling stability stems from the "free" space provided by the TFA compartment with intrinsic porosity (cf. Figure S40, Supporting Information), suggesting the robustness of the TFA as an anode material for full cells. By comparing these results with current research on ASSLBs (Table S4, Supporting Information), the TFA material used in this study demonstrates significant advantages in terms of high areal capacity and high current densities (Figure 6e). These results further testify the feasibility of the TFA concept in improving the performance of ASSLBs under extreme working conditions (e.g., external pressure, current density, and areal capacity), which are critical for achieving high energy density in practical cells (Table S5, Supporting Information).

3. Conclusion

In summary, the TFA concept is proposed to mitigate detrimental effects caused by non-electroactive phases in anodes. The effectiveness of this strategy is validated through a tailored Li–B alloy featuring a fibrous Li_5B_4 skeleton and an optimized Li° phase. The TFA-based symmetric cell shows significantly improved electrochemical performance compared to pristine Li° cells, along with strong tolerance toward external pressure (0–50 MPa). Specifically, the symmetric cell achieves a maximum CCD of 5.8 mA·cm^{-2} and maintains stable cycling for 6,000 h at a capacity of 2 mAh·cm^{-2}. When paired with an FeS_2 cathode under 40 MPa external pressure, the TFA-based full cell shows an excellent cycling performance, retaining 70% capacity after 800 cycles at a current density of 3.07 mA·cm^{-2}. The full cell further demonstrates stable cycling at a high reversible capacity of 9.5 mAh·cm^{-2}, corresponding to 62% utilization of the anode. Additionally, when paired with an NCM cathode at 5 MPa external pressure, the TFA-based full cell also exhibits excellent rate and cycling performance. These impressive advancements are powered by the TFA's 3D fibrous skeleton, which provides robust mechanical strength to maintain anode structural integrity and lithiophilic nature for accelerating lithium transport. The TFA concept not only opens a promising pathway for high-energy ASSLBs but also inspires the architectural design of electrode materials in emerging solid-state battery systems (e.g., Na^+, K^+, Ca^{2+}).

4. Experimental Section

Synthesis of Electrolyte: To prepare Li_6PS_5Cl (LPSCl) powder, lithium sulfide (Li_2S, 99.9%, Alfa Aesar), phosphorus pentasulfide (P_2S_5, 99%, Aladdin Chemistry), and lithium chloride (LiCl, 99.9%, Sigma–Aldrich) were used as starting materials. These samples were weighed in stoichiometric proportions and placed into an agate ball mill jar for grinding using a planetary ball mill (Retch, PM400). The resulting mixture was then annealed in an alumina crucible at 550 °C for 2 h to form LPSCl electrolyte. After sintering, the product was ground in an agate mortar and pestle for at least 15 min to achieve a uniform LPSCl powder.

Synthesis of Anode: The pristine Li° and TFA materials, both supplied by China Energy Lithium Co., Ltd, exhibited an average thickness of 100 µm. The TFA material was synthesized through a carefully controlled thermal reaction process involving stoichiometric lithium and boron in an iron crucible under an argon atmosphere. The synthesis occurs in two distinct stages:[31] 1) low-temperature stirring phase (300–400 °C): molten lithium was thoroughly mixed with boron powder, initiating an exothermic reaction (ΔT ≈ 330 °C) that produces an amorphous LiB_3 intermediate phase. 2) high-temperature reaction phase (500–700 °C): Subsequent heating triggers a second exothermic reaction (ΔT ≈ 530 °C), dissolving the LiB_3 phase and forming the characteristic fibrous Li_5B_4 framework.[32] This synthesis protocol has been specifically optimized for ASSLB applications through precise control of the skeleton architecture and free Li° content. The commercial-scale production of this tailored TFA material was currently available through China Energy Lithium Co., Ltd.

Preparation of Cathode: To prepare the $LiNi_{0.93}Co_{0.06}Mn_{0.01}O_2$ (NCM) composite cathode, 70 wt.% NCM and 30 wt.% LPSCl were mixed evenly in a mortar for 30 min. NCM powder was prepared using the $Ni_{0.93}Co_{0.06}Mn_{0.01}(OH)_2$, $LiOH{\cdot}H_2O$ and a small amount of Nb_2O_5 additive at 800 °C for 15 h in a flowing oxygen atmosphere using a tube furnace. The FeS_2 composite cathode was obtained by blending FeS_2 with Vapor grown carbon fiber (VGCF) and LPSCl with a weight ratio of 4:3:1.5. The mixing process was achieved by the ball milling method. The above synthesis process was carried out under an argon atmosphere in the glove box to avoid air reacting with the solid-state electrolytes.

The Extraction of "Free" Lithium in TFA: Soaking TFA in a tetrahydrofuran (THF) solution containing 8 wt.% naphthalene effectively removes free lithium phases. The underlying reaction mechanism involves the interaction of alkali metals with unsaturated aromatic compounds, such as naphthalene, in polar aprotic solvents like dimethyl ether or THF, leading to the formation of aromatic radical anions.[33] The TFA material was immersed in this solution for 24 h until the solution remains clear and colorless, indicating completion of the reaction. The resulting TFA skeleton was then rinsed with THF to remove any residual naphthalene.

Materials Characterization: Powder X-ray diffraction (XRD) tests were performed on a Bruker X-ray diffractometer (Bruker AXS D8 Advance) using Cu K_α radiation ($\lambda = 1.5406$ Å). The diffraction data were collected in the 2θ (θ = incident X-ray angle) range from 10° to 90° and the diffractometer operating at 40 kV and 40 mA. Field-emission Scanning electron microscopy (SEM, Hitachi 8100) with an implemented energy dispersive spectrometer (EDS) was used to provide morphological information for all samples, which was operated at 15 kV. An atomic force microscope (AFM, Dimension icon, Bruker) was used to characterize the surface morphology and Derjaguin–Muller–Toporov (DMT) modulus were obtained using the PeakForce QNM mode with an RTESPA-525 probe. Computed tomography (CT) scans were conducted using a ZEISS Xradia 610 Versa (Carl Zeiss X-ray Microscopy Inc.) at a voltage of 50 kV with a resolution of 0.3 µm. The resulting CT images were reconstructed using Dragonfly software (Object Research Systems Inc.). Time-of-flight second ion mass spectroscopy (ToF-SIMS, ION TOF SIMS 5) was used for component analysis of lithium diffusivity in different anodes under ultrahigh vacuum (below 10^{-7} mbar). Secondary ions with negative polarity were detected and analyzed using a pulsed 30 keV Bi^+ (9 ns)-ion beam for spectrum and depth profiling in the non-interlaced mode. A Cs^+ ion beam (1 keV) was used for sputtering the electrodes.

Computational Methods: All results of calculations in this work were performed in the framework of the density functional theory (DFT) with the projector augmented plane-wave method, as implemented in the Vienna ab initio simulation package (VASP).[34] The generalized gradient approximation proposed by Perdew–Burke–Ernzerhof (PBE), was selected for the exchange-correlation potential.[35] The cut-off energy for a plane wave was set to 480 eV. The energy criterion was set to 10^{-5} eV in the iterative solution of the Kohn-Sham equation. All the structures were relaxed until the residual forces on the atoms have declined to less than 0.02 eV $Å^{-1}$. The Li adsorption energy E_{adsorb} is described as follows (Equation 1):[36]

$$E_{adsorb} = E_{slab+Li} - E_{slab} - E_{Li} \quad (1)$$

in which, the $E_{slab+Li}$ is the total energy of the slab structure with one Li adsorbed on the surface; E_{slab} and E_{Li} are the energies of the slab structure and one Li.

Meanwhile, to study the ion transport, ab initio molecular dynamics (AIMD) simulations were performed using a canonical ensemble (NVT) with a $1 \times 1 \times 1$ k-point and a time step of 2 fs. The simulation temperature was controlled using a Nose-Hoover thermostat.[37]

Lithium Diffusivity Measured by SIMS: ^{6}Li-enriched lithium metal (95 at.% ^{6}Li, CIL) was employed for isotopic tracing and was hereinafter referred to as ^{6}Li, in contrast to lithium metal granules with a natural isotopic ratio, predominantly ^{7}Li. The ^{6}Li (100 µm) layer was laminated with TFA or Li° anode, and SIMS was utilized to ascertain the diffusion concentration of ^{6}Li in various anodes. The diffusion profiles were fitted to the Gaussian solution of Fick's second law for a thin film:

$$C(x, t) = \frac{N}{\sqrt{\pi D t}} e^{-x^2/4D_{Li}t} \quad (2)$$

Here, $C(x, t)$ represents the excess lithium isotope concentration relative to the background concentration at position x and time t. N was the total amount of the diffusing species, given by the integral $N = \int_0^\infty c(x, t)dx$, and D_{Li} was the diffusion coefficient.[38] This solution was applicable for isotope diffusion experiments involving a fixed quantity of diffusing species, such as those conducted in thin film configurations.

Electrochemical Characterization: All the preparation processes were performed in an argon-filled glove box with $O_2 < 0.1$ ppm, $H_2O < 0.1$ ppm (Lab Star, Mbraun, Germany). For symmetric cells, 150 mg of LPSCl powder was placed in a mold cell (10 mm in diameter) and pressed under 360 MPa for 2 min. Then, Li film (100 µm) or TFA film (100 µm) was placed on both sides of the electrolyte, and stainless-steel foils were introduced as current collectors by pressing under 50 or 360 MPa. For full cells, first, 150 mg of LPSCl powder was placed in a mold cell (10 mm in diameter) and pressed under 360 MPa for 2 min. Second, the composite cathode powder (NCM or FeS_2) was uniformly spread on the electrolyte pellet and pressed under 360 MPa (≈3 min). Finally, the Li film or TFA film was attached, and stainless-steel foils were introduced as current collectors by pressing under 50 or 360 MPa. Galvanostatic charge–discharge was conducted via battery test system at 80 °C for symmetric cells and FeS_2 full cells or at room temperature for NCM full cells. (LAND CT-2001A, Wuhan Rambo Electronics Co., Ltd.).

In Situ Pressure Monitoring: Control of the external pressure applied to the solid-state cells during cycling was conducted with a special cell holder. A 50 kN load cell was mounted at the bottom of the holder along the axis of the battery. The bottom of the solid-state cells was in direct contact with the load cell. The external pressure could be accurately tuned by tightening the nuts accordingly.

In Situ Electrochemical Impedance Spectroscopy: EIS was used to detect impedance changes operando during current load. Current densities of 0.5 mA cm^{-2} were used. Measurements were performed using an impedance analyzer (Solartron, 1470E) at frequencies from 1 MHz to 0.01 Hz in an argon atmosphere.

Supporting Information

Supporting Information is available from the Wiley Online Library or from the author.

Acknowledgements

X.Z. and H.Y. contributed equally to this work. The work was supported by the National Key R&D Program of China (Grant no. 2022YFB3807700), the National Natural Science Foundation of China (Grant no. 22479166, 22309194, 52372244, 22322903, 22179144), and the Youth Innovation Promotion Association CAS (Grant no. Y2023009, Y2021080).

Conflict of Interest

The authors declare no conflict of interest.

Data Availability Statement

The data that support the findings of this study are available from the corresponding author upon reasonable request.

Keywords

3D skeleton, all-solid-state lithium battery, lithium dendrite, lithium metal anode, topology fortified

Received: April 2, 2025
Revised: May 2, 2025
Published online: May 19, 2025

[1] a) S. Chen, F. Dai, M. Cai, *ACS Energy Lett.* **2020**, *5*, 3140; b) J. W. Choi, D. Aurbach, *Nat. Rev. Mater.* **2016**, *1*, 16013; c) D. Lin, Y. Liu, Y. Cui, *Nat. Nanotechnol.* **2017**, *12*, 194.

[2] a) L.-Z. Fan, H. He, C.-W. Nan, *Nat. Rev. Mater.* **2021**, *6*, 1003; b) L. Porz, T. Swamy, B. W. Sheldon, D. Rettenwander, T. Froemling, H. L. Thaman, S. Berendts, R. Uecker, W. C. Carter, Y.-M. Chiang, *Adv. Energy Mater.* **2017**, *7*, 1701003.

[3] a) B. L. Xiangwen Gao, B. Hu, Z. Ning, D. S. Jolly, S. Zhang, J. Perera, J. Bu, J. Liu, C. Doerrer, E.d Darnbrough, D. Armstrong, P. S. Grant, P. G. Bruce, *Joule* **2022**, *6*, 636; b) W. J. Li, M. Hirayama, K. Suzuki, R. Kanno, *Mater. Trans.* **2016**, *57*, 549; c) R. Koerver, I. Ayguen, T. Leichtweiss, C. Dietrich, W. Zhang, J. O. Binder, P. Hartmann, W. G. Zeier, J. Janek, *Chem. Mater.* **2017**, *29*, 5574.

[4] a) H. Wan, Z. Wang, W. Zhang, X. He, C. Wang, *Nature* **2023**, *623*, 739; b) G. V. Alexander, C. Shi, J. O'Neill, E. D. Wachsman, *Nat. Mater.* **2023**, *22*, 1136.
[5] a) H. H. Sun, H. H. Ryu, U. H. Kim, J. A. Weeks, A. Heller, Y. K. Sun, C. B. Mullins, *ACS Energy Lett.* **2020**, *5*, 1136; b) B. J. Hwang, Y. W. Tsai, D. Carlier, G. Ceder, *Chem. Mater.* **2003**, *15*, 3676; c) L. P. Wang, H. Li, X. J. Huang, E. Baudrin, *Solid State Ionics* **2011**, *193*, 32.
[6] a) J. Zhou, M. L. Holekevi Chandrappa, S. Tan, S. Wang, C. Wu, H. Nguyen, C. Wang, H. Liu, S. Yu, Q. R. S. Miller, G. Hyun, J. Holoubek, J. Hong, Y. Xiao, C. Soulen, Z. Fan, E. E. Fullerton, C. J. Brooks, C. Wang, R. J. Clément, Y. Yao, E. Hu, S. P. Ong, P. Liu, *Nature* **2024**, *627*, 301; b) X. Li, J. Liang, J. Luo, C. Wang, X. Li, Q. Sun, R. Li, L. Zhang, R. Yang, S. Lu, H. Huang, X. Sun, *Adv. Mater.* **2019**, *31*, 1808100.
[7] a) X. X. Zhu, L. G. Wang, Z. Y. Bai, J. Lu, T. P. Wu, *Nano-Micro Lett.* **2023**, *15*, 75; b) L. Wang, Z. Wu, J. Zou, P. Gao, X. Niu, H. Li, L. Chen, *Joule* **2019**, *3*, 2086; c) Z. Li, G. Zhou, S. Li, H. Liu, L. Wang, H. Li, *Joule* **2023**, *7*, 2609.
[8] a) X. Hu, Z. Zhang, X. Zhang, Y. Wang, X. Yang, X. Wang, M. Fayena-Greenstein, H. A. Yehezkel, S. Langford, D. Zhou, B. Li, G. Wang, D. Aurbach, *Nat. Rev. Mater.* **2024**, *9*, 305; b) S. Puls, E. Nazmutdinova, F. Kalyk, H. M. Woolley, J. F. Thomsen, Z. Cheng, A. Fauchier-Magnan, A. Gautam, M. Gockeln, S.-Y. Ham, M. T. Hasan, M.-G. Jeong, D. Hiraoka, J. S. Kim, T. Kutsch, B. Lelotte, P. Minnmann, V. Miß, K. Motohashi, D. L. Nelson, F. Ooms, F. Piccolo, C. Plank, M. Rosner, S. E. Sandoval, E. Schlautmann, R. Schuster, D. Spencer-Jolly, Y. Sun, B. S. Vishnugopi, et al., *Nat. Energy* **2024**, *9*, 1310.
[9] T. Krauskopf, F. H. Richter, W. G. Zeier, J. Janek, *Chem. Rev.* **2020**, *120*, 7745.
[10] a) H. Yan, K. Tantratian, K. Ellwood, E. T. Harrison, M. Nichols, X. Cui, L. Chen, *Adv. Energy Mater.* **2022**, *12*, 2102283; b) J. M. Doux, H. Nguyen, D. H. S. Tan, A. Banerjee, X. Wang, E. A. Wu, C. Jo, H. Yang, Y. S. Meng, *Adv. Energy Mater.* **2019**, *10*, 1903253.
[11] a) M. Wang, J. B. Wolfenstine, J. Sakamoto, *Electrochim. Acta* **2019**, *296*, 842; b) K. H. Kim, M.-J. Lee, M. Ryu, T.-K. Liu, J. H. Lee, C. Jung, J.-S. Kim, J. H. Park, *Nat. Commun.* **2024**, *15*, 3586; c) J. Kasemchainan, S. Zekoll, D. Spencer Jolly, Z. Ning, G. O. Hartley, J. Marrow, P. G. Bruce, *Nat. Mater.* **2019**, *18*, 1105.
[12] X. Hu, J. Yu, Y. Wang, W. Guo, X. Zhang, M. Armand, F. Kang, G. Wang, D. Zhou, B. Li, *Adv. Mater.* **2023**, *36*, 2308275.
[13] a) J. A. Lewis, K. A. Cavallaro, Y. Liu, M. T. McDowell, *Joule* **2022**, *6*, 1418; b) B. Hertzberg, J. Benson, G. Yushin, *Electrochem. Commun.* **2011**, *13*, 818; c) C. S. Hong, S. M. Han, *Ext. Mech. Lett.* **2020**, *40*, 100907; d) W.-J. Zhang, *J. Power Sources* **2011**, *196*, 13; e) W. Yan, Z. Mu, Z. Wang, Y. Huang, D. Wu, P. Lu, J. Lu, J. Xu, Y. Wu, T. Ma, M. Yang, X. Zhu, Y. Xia, S. Shi, L. Chen, H. Li, F. Wu, *Nat. Energy* **2023**, *8*, 800; f) J. Zhu, J. Luo, J. Li, S. Huang, H. Geng, Z. Chen, L. Jia, Y. Fu, X. Zhang, X. Zhuang, *Adv. Mater.* **2024**, *36*, 2407128.
[14] a) L. A. Berla, S. W. Lee, Y. Cui, W. D. Nix, *J. Power Sources* **2015**, *273*, 41; b) J. Aspinall, Y. Chart, H. Guo, P. Shrestha, M. Burton, M. Pasta, *ACS Energy Lett.* **2024**, *9*, 578.
[15] a) Z.-X. Wang, Y. Lu, C.-Z. Zhao, W.-Z. Huang, X.-Y. Huang, W.-J. Kong, L.-X. Li, Z.-Y. Wang, H. Yuan, J.-Q. Huang, Q. Zhang, *Joule* **2024**, *8*, 2794; b) L. Ye, Y. Lu, Y. Wang, J. Li, X. Li, *Nat. Mater.* **2024**, *23*, 244.
[16] B. T. Heligman, A. Manthiram, *ACS Energy Lett.* **2021**, *6*, 2666.
[17] a) X. L. Zhang, W. K. Wang, A. B. Wang, Y. Q. Huang, K. G. Yuan, Z. B. Yu, J. Y. Qiu, Y. S. Yang, *J. Mater. Chem. A* **2014**, *2*, 11660; b) H.-F. Huang, Y.-N. Gui, F. Sun, Z.-J. Liu, H.-L. Ning, C. Wu, L.-B. Chen, *Rare Met.* **2021**, *40*, 3494.
[18] W. P. Kilroy, I. Angres, *J. Less-Common Met.* **1979**, *63*, 123.
[19] H. B. Borgstedt, C. Guminski, *J. Phase Equilib.* **2003**, *24*, 572.
[20] a) X. Wu, H. Pan, M. Zhang, H. Zhong, Z. Zhang, W. Li, X. Sun, X. Mu, S. Tang, P. He, H. Zhou, *Adv. Sci.* **2024**, *11*, 2308604; b) Q.-K. Zhang, X.-Q. Zhang, J. Wan, N. Yao, T.-L. Song, J. Xie, L.-P. Hou, M.-Y. Zhou, X. Chen, B.-Q. Li, R. Wen, H.-J. Peng, Q. Zhang, J.-Q. Huang, *Nat. Energy* **2023**, *8*, 725.
[21] a) G. Wang, B. Xu, J. Shi, M. Wu, H. Su, C. Ouyang, *Nanoscale* **2019**, *11*, 14042; b) F. Fu, X. Wang, L. Zhang, J. Chen, B. Xu, C. Ouyang, S. Xu, F.-Z. Dai, E. Weinan, *Adv. Funct. Mater.* **2023**, *33*, 2303936.
[22] a) M. Z. Hui Pan, Z. Cheng, H. Jiang, J. Yang, P. Wang, *Sci. Adv.* **2022**, *8*, abn4372; b) S. Zhang, J. Chen, C. Zhu, Q. Liu, Q. Li, R. Liu, X. Jiang, Y. Yan, S. Sun, L. Yin, R. Wang, *ACS Nano* **2023**, *17*, 24290.
[23] a) L. Fu, M. Wan, B. Zhang, Y. Yuan, Y. Jin, W. Wang, X. Wang, Y. Li, L. Wang, J. Jiang, J. Lu, Y. Sun, *Adv. Mater.* **2020**, *32*, 2000952; b) C. Wu, H. Huang, W. Lu, Z. Wei, X. Ni, F. Sun, P. Qing, Z. Liu, J. Ma, W. Wei, L. Chen, C. Yan, L. Mai, *Adv. Sci.* **2020**, *7*, 1902643; c) X.-B. Cheng, H.-J. Peng, J.-Q. Huang, F. Wei, Q. Zhang, *Small* **2014**, *10*, 4257.
[24] a) S. Sarkar, V. Thangadurai, *ACS Energy Lett.* **2022**, *7*, 1492; b) H. Shen, E. Yi, L. Cheng, M. Amores, G. Chen, S. W. Sofie, M. M. Doeff, *Sustain. Energy Fuels* **2019**, *3*, 1647.
[25] H. Huo, J. Gao, N. Zhao, D. Zhang, N. G. Holmes, X. Li, Y. Sun, J. Fu, R. Li, X. Guo, X. Sun, *Nat. Commun.* **2021**, *12*, 176.
[26] S.-Y. Ham, H. Yang, O. Nunez-cuacuas, D. H. S. Tan, Y.-T. Chen, G. Deysher, A. Cronk, P. Ridley, J.-M. Doux, E. A. Wu, J. Jang, Y. S. Meng, *Energy Storage Mater.* **2023**, *55*, 455.
[27] Z. Chen, Z. Liang, H. Zhong, Y. Su, K. Wang, Y. Yang, *ACS Energy Lett.* **2022**, *7*, 2761.
[28] a) J. K. Eckhardt, T. Fuchs, S. Burkhardt, P. J. Klar, J. Janek, C. Heiliger, *ACS Appl. Mater. Interfaces* **2022**, *14*, 42757; b) J. K. Eckhardt, T. Fuchs, S. Burkhardt, P. J. Klar, J. Janek, C. Heiliger, *Adv. Mater. Interfaces* **2023**, *10*, 2202354.
[29] a) X. T. Qian, Y. Lyu, S. Y. Zhou, Y. C. Qiu, Y. Sun, Y. Yuan, M. H. Shao, *Adv. Mater.* **2024**, *36*, 2412319; b) M. Z. Hui Pan, Z. Cheng, H. Jiang, J. Yang, P. Wang, P. He, H. Zhou, *Sci. Adv.* **2022**, *8*, abn4372.
[30] E. Rangasamy, J. C. Li, G. Sahu, N. Dudney, C. D. Liang, *J. Am. Chem. Soc.* **2014**, *136*, 6874.
[31] S. S. Frederick, E. Wang, Md., U.S, Patent 4110111 , **1978**.
[32] a) A. Meden, J. Mavri, M. Bele, S. Pejovnik, *J. Phys. Chem.* **1995**, *99*, 4252; b) Z. J. Liu, X. H. Qu, Z. Y. Li, B. Y. Huang, *Sci. China Tech. Sci.* **2003**, *46*, 391.
[33] Z. Song, M. Tian, J. Zhu, J. Chen, W. Feng, L. Ben, H. Yu, X. Huang, M. Armand, Z. Zhou, H. Zhang, *Adv. Mater.* **2024**, *36*, 2410954.
[34] G. Kresse, J. Furthmuller, *Phys. Rev. B* **1996**, *54*, 11169.
[35] a) J. P. Perdew, K. Burke, M. Ernzerhof, *Phys. Rev. Lett.* **1997**, *78*, 1396; b) J. P. Perdew, M. Ernzerhof, K. Burke, *J. Chem. Phys.* **1996**, *105*, 9982.
[36] a) J. Cao, Y. Shi, A. Gao, G. Du, M. Dilxat, Y. Zhang, M. Cai, G. Qian, X. Lu, F. Xie, Y. Sun, X. Lu, *Nat. Commun.* **2024**, *15*, 1354; b) Y. Li, J. Li, H. Xiao, T. Xie, W. Zheng, J. He, H. Zhu, S. Huang, *Adv. Funct. Mater.* **2023**, *33*, 2213905.
[37] S. Nose, *J. Chem. Phys.* **1984**, *81*, 511.
[38] M. Siniscalchi, J. Liu, J. S. Gibson, S. J. Turrell, J. Aspinall, R. S. Weatherup, M. Pasta, S. C. Speller, C. R. M. Grovenor, *ACS Energy Lett.* **2022**, *7*, 3593.

